Correlation between shape and stray field in indented square nanomagnets: Experimental and theoretical study

Colin Rawlings,[1] Sigrid Weigelt,[1] Bingyan Hong,[2] Crispin H. Barnes,[2] Mark E. Welland,[1] and Colm Durkan[1,*]
[1]*Nanoscience Centre, University of Cambridge, J. J. Thomson Avenue, Cambridge CB3 0FF, United Kingdom*
[2]*Thin-Film Magnetism Group, Cavendish Laboratory, University of Cambridge, J. J. Thomson Avenue, Cambridge CB3 OHE, United Kingdom*
(Received 30 March 2010; revised manuscript received 29 June 2010; published 3 August 2010)

We have used the scanning probe technique, magnetic force microscopy (MFM), to study the magnetization distribution in a system of indented rectangles made from permalloy. An accurate linear approximation to the micromagnetic equations was implemented in commercial finite element software. This model was used to study the important effect of tip-sample interaction on our MFM measurements. Comparison between experiment and our model confirmed that even for large indents the nanomagnets adopted vortex ground states. A qualitative relationship between the sample's magnetization, in the absence of the MFM tip's magnetic field, and the induced contrast was identified. The optimum ratio of charge contrast to induced contrast when observing vortex states was found to be proportional to the tip moment raised to the power of 0.4. This was subject to the limitations imposed by resolution and thermal noise. It occurred for large separation between tip and sample.

DOI: 10.1103/PhysRevB.82.085404 PACS number(s): 75.75.−c, 85.70.Ay

I. INTRODUCTION

Nanoscale magnetic devices have rich potential both in memory storage[1] and computation.[2] The theoretical basis for such devices is well established; micromagnetics is experimentally successful on the nanometer and nanosecond scale.[3] The techniques developed by the semiconductor industry are in many cases applicable to the deposition of magnetic materials.[4] This aids device development and allows for the integration of nanomagnetic devices with complementary metal-oxide semiconductor circuitry.[1]

The atomic force microscope (AFM) is an important and flexible tool in the development of nanoscale devices. Use of a magnetically coated tip in an AFM, so called Magnetic Force Microscopy (MFM),[5] measures local magnetic fields with a resolution of better than 50 nm. Magnetic cantilevers are also employed in magnetic resonance force microscopy (MRFM).[6] MRFM studies the dynamic, nonequilibrium behavior of a magnetic sample, in contrast MFM probes the static magnetization distribution.

MFM systems may operate at atmospheric pressure thus allowing easy physical access, including electrical connection, to the sample during measurement. Consequently in many cases, MFM methods are better suited to probing magnetization in nanoscale devices than electron based alternatives, for example, Lorentz Microscopy,[7] or SEMPA (Scanning Electron Microscopy with Polarization Analysis).[8] These electron techniques require vacuum conditions and careful sample preparation.

The challenge with MFM lies in determining the magnetization distribution within a magnetic sample from a measurement taken tens of nanometers above it. The analysis of Hubert *et al.*[9] demonstrated that MFM contrast corresponds to the magnetic charge density directly below the tip. The magnetic charge density, ρ_m, is related to the magnetization distribution, $\mathbf{M}$, as: $\rho_m = -\nabla . \mathbf{M}$. This so called charge contrast is augmented by induced or susceptibility contrast in magnetically soft samples. Induced contrast is the contribution to the measured MFM signal arising from the disturbance of the magnetization by the magnetic field of the MFM tip. Soft magnetic materials such as permalloy currently offer the greatest potential for device applications. Thus it is important to understand induced contrast.

MFM does not therefore measure the sample magnetization directly and the act of measurement disturbs the sample due to the interaction of the tip stray field with the sample's magnetization. These factors make the prediction of MFM measurements for a given magnetization distribution an important part of the experimental process. Through comparison with these predictions the experimentally observed magnetization distribution can be established from its MFM "fingerprint." Any such prediction must account for the interaction of tip and sample. Several previous predictions of MFM contrast that included the effect of the tip on the sample have been made.[10,11] Such a process is computationally expensive as a separate micromagnetic problem must be solved at each tip position.

This paper outlines an accurate simulation method for predicting MFM images that has been implemented in commercial finite-element software. The method exploits the weak nature of the tip perturbation and the ability of the finite-element method to combine simultaneous partial differential equations (PDEs) into a single local (or equivalently sparse) problem. Using a standard Quad-Core desktop computer, results were obtained in roughly an hour. The method takes account of the perturbation of the magnetization by the field of the MFM tip. We compare our simulation results with experimental images taken on the system of indented rectangular prisms first studied by Koltsov and Welland in Ref. 12. The indentation was proposed by Koltsov as a means of controlling the formation of vortex states (see Sec. V A), a key issue in the design of storage elements for magnetic random access memory. The original investigation employed a magneto-optical Kerr magnetometer to measure the

hysteresis properties of arrays of indented rectangles. Our combined experimental and numerical MFM technique extended this work to the direct measurement of magnetization distributions in individual nanomagnets.

The simulation results provide insight into the relationship between the unperturbed magnetization state and the induced contrast. The results are used to explain several frequently observed artifacts in MFM measurements. Operating conditions that facilitate the interpretation of experimental images are also identified.

II. MICROMAGNETICS

The Maxwell Equations relevant to the steady flow of charge in free space are $\nabla . \mathbf{B} = 0$ and $\nabla \times \mathbf{B} = \mu_0 \mathbf{j}$. For fields in materials it is preferable to work with the spatial average of $\mathbf{B}$ over a mesoscopic length scale[13] and introduce the Magnetization, $\mathbf{M} \cdot \mathbf{M}$ is defined as the spatial average of the atomic magnetic moments. In the absence of macroscopic currents

$$\mathbf{B} = \mu_0(\nabla \phi_m + \mathbf{M}), \tag{1}$$

where

$$\nabla^2 \phi_m = -\nabla \cdot \mathbf{M} = \rho_m, \tag{2}$$

$$\Rightarrow \phi_m(\mathbf{x}) = \int_{\Omega_m} G(\mathbf{x},\mathbf{u})[-\nabla \cdot \mathbf{M}(\mathbf{u})] dV(\mathbf{u}) \tag{3}$$

G is the fundamental solution or Green's function for Poisson's equation. The vector field $\nabla \phi_m$ is conventionally termed $\mathbf{H}$.

Within the theory of Micromagnetics, equilibrium magnetization distributions minimize the value of the functional,[14] I, over the sample volume Ω_m

$$I[\mathbf{M}] = \int_{\Omega_m} \frac{A_{ex}}{M_s^2} \sum_{i=1}^{3} |\nabla M_i|^2 + w_{ani} - \mathbf{M} \cdot \left(\frac{\mu_0}{2} \mathbf{H}^{(m)} + \mathbf{B}^{(app)} \right) dV \tag{4}$$

subject to the constraint imposed by Eq. (2) and

$$|\mathbf{M}| = M_s, \tag{5}$$

where A_{ex} is the material exchange constant, M_s the saturation magnetization, and ω_{ani} is the material's anisotropy energy density. $\mathbf{B}^{(app)}$ is the externally applied magnetic field and $\mathbf{H}^{(m)}$ is the so-called stray field due to $\mathbf{M}$. Throughout this work we assume $\omega_{ani} \simeq 0$. The calculus of variations can be used to obtain the PDEs on $\mathbf{M}$ (Brown's equations[14]). These can take one of two forms depending on how constraint in Eq. (5) is handled. If $\mathbf{M}$ is described in terms of angular variables θ and ψ

$$\mathbf{M} = M_s(\cos\theta \cos\psi, \sin\theta \cos\psi, \sin\psi) \tag{6}$$

the constraint, Eq. (5), is satisfied. The equations governing θ and ψ can be expressed in terms of the nondimensional variables

$$\bar{x} = \frac{x}{a}, \quad H_i = \frac{H_i}{M_s}, \quad \bar{M}_i = \frac{M_i}{M_s}, \quad \bar{B}_i = \frac{B_i}{\mu_0 M_s}, \tag{7}$$

where a is the width of the structure and the overbar in Eq. (7) denotes that the variable is nondimensional.

$$\bar{\nabla} \cdot (-\cos^2\psi \bar{\nabla}\theta) = \frac{1}{2A} \bar{\mathbf{M}}_X' \cdot (\bar{\mathbf{H}}^{(m)} + \bar{\mathbf{B}}^{(app)}), \tag{8}$$

$$\bar{\nabla} \cdot (-\bar{\nabla}\psi) = \frac{1}{2} \sin 2\psi |\bar{\nabla}\theta|^2 + \frac{1}{2A} \bar{\mathbf{M}}_Y' \cdot (\bar{\mathbf{H}}^{(m)} + \bar{\mathbf{B}}^{(app)}), \tag{9}$$

where

$$\bar{\mathbf{M}}_X' = (-\sin\theta \cos\psi, \cos\theta \cos\psi, 0),$$

$$\bar{\mathbf{M}}_Y' = (-\cos\theta \sin\psi, -\sin\theta \sin\psi, \cos\psi),$$

$$A = \frac{A_{ex}}{a^2 \mu_0 M_s^2} = \frac{1}{2}\left(\frac{l_{ex}}{a}\right)^2$$

l_{ex} is the exchange length for the material and is defined as $l_{ex} = \sqrt{2A_{ex}/\mu_0 M_s^2}$.

Alternatively the PDE governing the components of the magnetization can be obtained. These will contain a Lagrange multiplier $\nu(\mathbf{x})$ corresponding to Eq. (5). In either case constraint in Eq. (2) remains active.

The starting point for our model of MFM systems is that it need only accurately predict small changes to the equilibrium magnetization. The change is caused by the application of the MFM tip's magnetic field to the sample, which thus changes $\mathbf{B}^{(app)}$ in Eq. (4). The difference between the equilibrium magnetization distributions before and after the tip field is applied, $\mathbf{M}_0$ and $\mathbf{M}_1$, respectively, is considered to have the property

$$|\delta\mathbf{M}/M_s| = |(\mathbf{M}_1 - \mathbf{M}_0)/M_s| \ll 1,$$

where $\delta\mathbf{M}$ does not satisfy this condition the tip field is strongly altering the magnetization of the sample. This means that the MFM measurement will not reflect the undisturbed distribution, $\mathbf{M}_0$, and under the chosen operating conditions the measurement is of little obvious value. Likewise the simulated MFM measurement is undoubtedly interesting but again of little practical value.

Using Eqs. (8) and (9) the equations governing the change in the magnetization can be obtained for $\delta\theta = \theta_1 - \theta_0$ and $\delta\psi = \psi_1 - \psi_0$. These have the general form

$$\nabla^2 \delta\theta = f_\theta(x, \delta\theta, \delta\psi, \theta_0, \psi_0, \delta\mathbf{B}^{(app)}) + \mathcal{O}(\delta\theta^2). \tag{10}$$

Given the considerations outlined above it is sufficient for our purposes to neglect terms of $\mathcal{O}(\delta\theta^2)$. Even neglecting second-order terms the expressions are rather lengthy and have been saved for Appendix A. The use of linear approximations to Eqs. (8) and (9) greatly increased the efficiency of the numerical solution (see Sec. IV A).

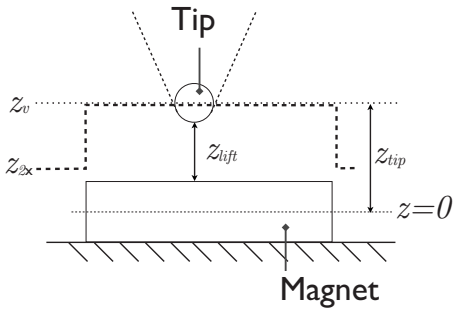

FIG. 1. Comparison of scan profile for the two pass technique ($z_{2\times}$) and the voltage regulation technique (z_v). The variables z_{tip} and z_{lift} are also defined.

III. MODEL FOR THE MFM SYSTEM

A. Microscope

Our numerical model was based around an atomic force microscope operating in a dynamic noncontact mode. In this regime the tip is scanned at a constant height above the surface. The height is made sufficiently large to ensure magnetic forces dominate the short-range electrostatic forces observed during AFM. The tip-sample separation can be achieved using a two pass technique, however, we treated the case where the separation between the tip and silicon substrate is kept constant.

This was achieved experimentally by applying a voltage between tip and sample. The consequent long-range electrostatic interaction applied a force to the tip which depended on the spatial average of the cantilever-surface separation. A feedback loop that regulates on the amplitude of cantilever oscillations adjusted the tip scan height such that the force gradient experienced by the tip was constant.

The advantage of the voltage regulation approach with respect to the two pass techniques is that the fine structure of the surface topography is not followed. As shown in Fig. 1 if the fine structure is followed the tip will rapidly approach the surface as it passes over the end of lithographically patterned features. Such rapid variation in tip height complicates interpretation of results particularly where surface charges have been deposited in the magnetic sample.

The tip force, f_m, due to the magnetic field results in a small change to the scan height, Δz. Where the applied electrostatic force is large, Δz is proportional to the measured gradient of the tip field.[15] As such it was this signal that is presented in the experimental MFM images of Sec. V.

Ignoring the edge effect associated with the two pass technique discussed previously, the simulated MFM results presented here are equally applicable to other dynamic MFM modes. Namely, measurement of the phase shift of oscillations or the resonant frequency of the cantilever since to first order both are proportional to the magnetic force gradient, f'_m. The only difference for these alternative MFM operating modes is in the calculation of the thermal noise floor. The thermal noise limit for phase shift detection is presented in Appendix B. The result for the amplitude shift case is functionally identical to the phase shift case provided the measurement bandwidth is taken as the cantilever mechanical bandwidth. It yields a minimum detectable force gradient of[16]

$$f'_{\min} = \frac{1}{\sqrt{\langle y_D^2 \rangle Q}} \sqrt{k_{can} k_B \Theta}, \tag{11}$$

where $\langle y_D^2 \rangle$ is the mean squared tip oscillation amplitude, Q is the quality factor of the cantilever, and k_{can} is its stiffness. k_B is the Boltzmann constant and Θ is the cantilever temperature.

B. Tip

The complex geometry of the MFM tip's magnetic coating was approximated as a sphere. The volume of the sphere was taken to be on the order of 10^5 nm^3.[17] It was assumed that the tip was coated with a hard magnetic material such that its magnetization was uniform. The tips were treated as being magnetized parallel to the tip axis. Conveniently the field from such a geometry contains only a dipole term in its multipole expansion. Material parameters appropriate to Cobalt were used.

Such a crude model for the tip can be defended on the basis of Hubert *et al.*'s[9] finding that tip geometry had increasingly little impact on higher order spatial derivatives of the tip field. The assumption of a sphere is much more accurate for single particle MFM tips,[18] where the coating is restricted to the very end of the tip. Neglecting the higher order multipole moments of the sample geometry can be further justified by their inevitable variability between tips.

C. Tip force

Our calculation of the tip force is conceptually different from those employed in previous numerical predictions of MFM contrast.[10,11] In these, gradients of the value of the functional, Eq. (4), were used to infer the tip force.

We proceed on the basis that magnetic fields are defined in terms of the forces they exert on charged particles. Thus no differencing is needed to establish the tip force and the fact that the constraint $|\mathbf{M}|=M_s$ implies the tip-sample system is not isolated need not be confronted.[19] For a steady current distribution the net force acting on a volume Ω_m is obtained from the Lorentz force as

$$\mathbf{F} = \int_{\Omega_m} \mathbf{j} \times \mathbf{B} dV. \tag{12}$$

Provided $\mathbf{B}$ can be accurately approximated by a first-order Taylor expansion over Ω_m the force on the current distribution simplifies to[13]

$$F_i = \sum_{l=1}^{3} m_l \frac{\partial B_l^{(app)}}{\partial x_i}, \tag{13}$$

where $\mathbf{m}$ is the dipole moment of the current distribution and $\mathbf{B}^{(app)}$ is the magnetic field applied to that distribution.[20] For a uniformly magnetized volume with surface $\partial\Omega$ the force is given by

$$\mathbf{F} = \oint_{\partial\Omega} (\mathbf{M}\cdot\mathbf{n})\mathbf{B}^{(app)} dS. \tag{14}$$

This can be used when the point dipole approximation[21] is inappropriate.[22] We neglected the tilt of the cantilever as well as nonlinearities in the force. Thus for a z axis aligned with the normal for the silicon surface (see Fig. 1) $f_m = \mathbf{F}.\mathbf{k}$ and $f'_m = \frac{\partial f_m}{\partial z_{tip}}$.

IV. METHOD

A. Numerical model

The MFM measurement was simulated in two stages. In the first stage the full micromagnetic problem was solved once to yield the equilibrium state of the magnetization, $\mathbf{M}_0$, for $\mathbf{B}^{(app)}=0$. The perturbation free or charge contrast could then be established from the resulting stray field $\mathbf{H}_0^{(m)}$. In the second stage the perturbation of the ground state was solved for each tip position. The results from the second stage allowed the calculation of the induced contrast. The commercial software package, COMSOL MULTIPHYSICS, was used to solve the PDEs. The process was automated using the "COMSOL with MATLAB" interface which allowed the solver to be controlled from the MATLAB programming suite.

The COMSOL package solved the equations outlined in Sec. II using the finite element method (FEM). The FEM is better suited to complex geometries and in particular does not introduce the edge roughness of techniques based around a finite difference (FD) discretization. Considerable effort is required to prevent the artificial roughness of the FD discretization from adversely effecting the simulation results.[23]

The FEM is a direct variational method which represents the continuous solution of the variational problem using a set of piecewise continuous interpolation functions. These interpolation functions are scaled by the solution values, $a_i = [\mathbf{a}]_i$. The value of $\mathbf{a}$ is found by imposing the Galerkin condition, which is equivalent to the condition $\frac{\partial I}{\partial a_i}=0$ for each element of $\mathbf{a}$.[24] The interpolation scheme and subsequent application of the Galerkin condition converts the PDE problem into a single sparse matrix equation on $\mathbf{a}$, $K\mathbf{a}=\mathbf{f}$. The computational effort involved in solving such problems numerically scales as $\mathcal{O}(N)$, where N is the number of elements of $\mathbf{a}$.

In the case of the perturbation problem where only the linear terms in Eq. (10) are retained the aim is to solve simultaneously the three PDEs on ϕ_m, $\delta\theta$, and $\delta\psi$ [Eqs. (2), (A1), and (A2)]. Using the FEM these individual equations can be assembled into a single matrix equation. In this way our solution of the perturbation problem was more efficient than general micromagnetic solvers based on the FEM.[25–27] These solvers employ direct search techniques to identify stationary points of the functional [Eq. (4)]. As such they require multiple solutions of the magnetostatic problem and then subsequent evaluation of the functional. In our model the perturbation problem was solved in a single step. For the solution of the ground state, $\mathbf{M}_0$, where the full micromagnetics problem had to be solved our numerical method was no more efficient than existing techniques.

The FEM as applied to simultaneous PDEs is analogous to the use of the combined functionals proposed by Asselin and Thiele[28] as implemented by Koehler *et al.*[25,29] Such an approach makes the problem local in character. In our case the details of the functionals were left to the commercial PDE solver. It is worth highlighting that we did not encounter a difficulty using the scalar potential rather than the magnetic vector potential, $\mathbf{A}$, where $\mathbf{B}=\nabla\times\mathbf{A}$. When using the $\{\phi_m,\mathbf{M}\}$ functional in Ref. 28 as the basis for an optimization routine Koehler *et al.*, encountered difficulties with convergence. This is because the $\{\phi_m,\mathbf{M}\}$ functional is a maximum with respect to ϕ_m and a minimum with respect to $\mathbf{M}$. However, in our case even for the full nonlinear problem where it was necessary to search for solutions the PDE solver was content to solve on ϕ_m and not $\mathbf{A}$. As such we could reduce the number of degrees of freedom needed for the magnetostatic problem by $\frac{1}{3}$.

For the solution of the full micromagnetic problem it was necessary to solve on the components of the magnetization vector rather than on θ and ψ. This was to allow for vortex states. In the representation of these states at some point during the orbit of a vortex core the value of θ must switch from 2π to 0. Such a discontinuity is not admitted in solutions obtained from the FEM. A satisfactory combination of speed and accuracy was achieved applying the constraint in Eq. (5) at the finite element nodes. A Kelvin transform[30] was used to handle the open boundary nature of the magnetostatic problem.

Calculation of the force gradient on the MFM tip requires evaluating a third order derivative of the magnetostatic potential. Numerical differentiation of such a high order on the finite-element solution for ϕ_m would have resulted in a low-quality estimate of the tip force. As an alternative we calculated the derivatives by differentiating Eq. (3) to yield

$$\frac{\partial^2\phi_m}{\partial x^2} = \int_{\Omega_m} \frac{\partial^2 G}{\partial x^2}[-\nabla\cdot\mathbf{M}(\mathbf{u})]dV. \tag{15}$$

The integral kernel $\frac{\partial^2 G}{\partial x^2}$ was evaluated analytically. Once the magnetization distribution in equilibrium with the field had been determined Eq. (15) was evaluated numerically over the finite-element mesh. The calculated field was only required at the tip location thus the computational effort scaled linearly with the number of degrees of freedom. Consequently it did not worsen the overall scaling behavior of our model.

B. Experimental technique

We performed MFM measurements on a system of prisms we refer to as indented rectangles.[12] The geometry of an indented rectangle is defined by the thickness, the width and the degree of indent (see Fig. 2). Structures were fabricated with thicknesses of 10 and 20 nm, and widths of 300 and 500 nm. Structures with both positive and negative indentations were fabricated. We refer to structures with negative indentations as elongated rectangles.

The samples were prepared by high-resolution electron-beam patterning of a bilayer of polymethyl methacrylate developed for 20 s in a 3:7 water/isopropanol solution. The permalloy ($Ni_{80}Fe_{20}$) was evaporated onto the patterns by

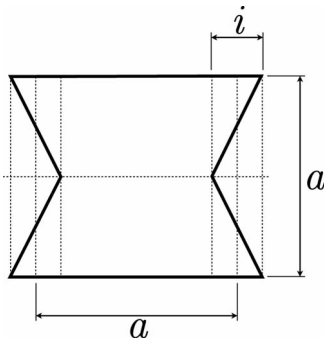

FIG. 2. Indented rectangle of width a and positive indent i.

e-beam evaporation in an ultrahigh vacuum system with a base pressure of 2×10^{-10} mBar. Furthermore a 4-nm gold capping layer was evaporated to prevent oxidation. Lift off was carried out in acetone.

V. RESULTS

As discussed in Sec. II we treated the magnetization distribution in the presence of the tip's magnetic field as the sum of the unperturbed magnetization, $\mathbf{M}_0$, and an induced change to that ground state, $\delta\mathbf{M}$. Since Eqs. (3) and (12) are linear with respect to $\mathbf{M}$ the tip force can be similarly decomposed into a perturbation free and induced part.

The origin for our coordinate system was placed at the center of the magnetic samples with the z axis pointing upwards towards the tip. The lift height (z_{lift}) was defined as the distance between the bottom of the tip and the top of the sample (see Fig. 1). The tip was assumed to have an effective volume of 10^5 nm^3 and saturation magnetization equal to that of Cobalt ($\mu_0 M_s$=1.8 T). The magnetic samples were attributed the properties of permalloy (l_{ex}=5.7 nm, $\mu_0 M_s$ =1 T, $\omega_{ani}\simeq 0$). Except where specifically identified as results from the full numerical model all MFM simulation data was obtained from the linear approximation to the micromagnetic equations.

A. Vortex state on a 500 nm square

A scanning electron microscope (SEM) image of a 20-nm-thick square magnet with 500 nm sides is shown in Fig. 3(a). The limitations of the patterning process result in a chamfer on the corners that has a radius of approximately 50 nm. This was included in all numerical simulations. Figure 3(b) shows an equilibrium magnetization distribution on the z=0 (central) plane. This type of magnetization distribution is known as a vortex or curling mode. The vortex core is visible as a dark region in the center of the structure. We refer to the sense of magnetization circulation around the core as the vortex's chirality [counterclockwise in Fig. 3(b)]. The variation in M_z with radius is shown in Fig. 3(c). We describe the direction that the magnetization points in the center of the core as the vortex's polarity. In the absence of applied fields all four combinations of chirality and polarity have equal energy. It can be seen in Fig. 3(c) that our numerical model reproduces the variation and core radius found by Scholz *et al.*[31]

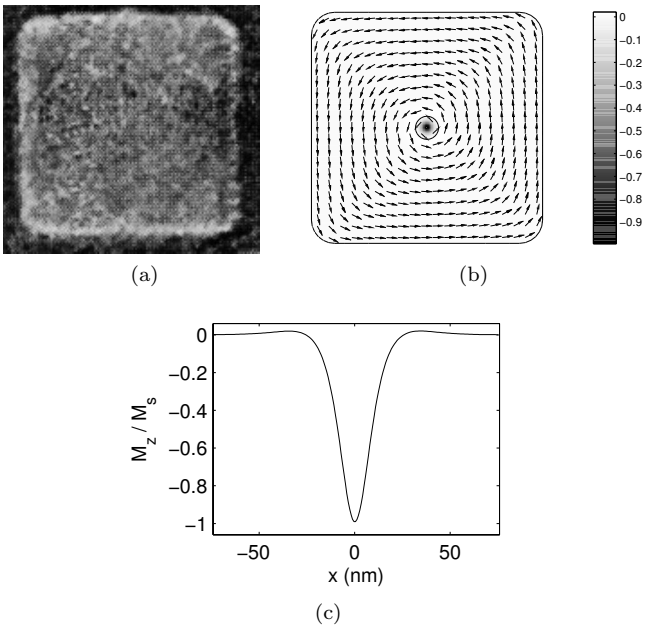

FIG. 3. Geometry of and magnetization in a square Permalloy magnet (width=500 nm, thickness=20 nm). (a) SEM image of geometry. (b) Equilibrium magnetization for $\mathbf{B}^{(app)}$=0 (color map: M_{z0}/M_s, arrows: $\mathbf{M}_0$). (c) $M_z(x)$ in vortex core along the line y =0, z=0.

Figure 4 compares the induced change in magnetization as calculated by the linearized model and the full micromagnetic model used to obtain the equilibrium states. The induced out of plane rotation of the magnetization for the two simulation methods is shown for a single tip location. The point in the figure directly beneath the tip is marked by an asterisk. Figure 5 shows the total force on the tip as it is scanned along the cross section marked by a dashed line in Fig. 4. The calculated force in the absence of tip perturbation is also included in Fig. 5 (dashed line).

Although the agreement between the two sets of results in Fig. 4 is good in the region beneath the tip there is significant error in the vicinity of the vortex core. This is because the linear model does not capture the tendency of the core to move under the in-plane field of the tip. This disagreement is magnified by the rapid variation in magnetization with position within the vortex core. This limitation of the linear approach is discussed further in Sec. VI D.

The agreement between the calculated values of f_m for the MFM tip as it is scanned along the black dashed line in Fig. 4 is better than 10% of the peak force. The induced component of the force on the tip is in the $-z$ direction as can be seen by comparing the total f_m with the perturbation free value. This is consistent with the tendency of magnetic dipoles to align with externally applied fields resulting in an attractive force between tip and sample.

Figure 6 presents a series of color maps relevant to the simulation of the MFM scan for the square magnet. The perturbation free and induced components of the scan signal are shown in Figs. 6(b) and 6(d), respectively. Figure 6(a) shows a plot of the magnetic charge density in the ground state. The quantity, $-M_{x0}H_{x0}^{(m)}-M_{y0}H_{y0}^{(m)}$, which we define as

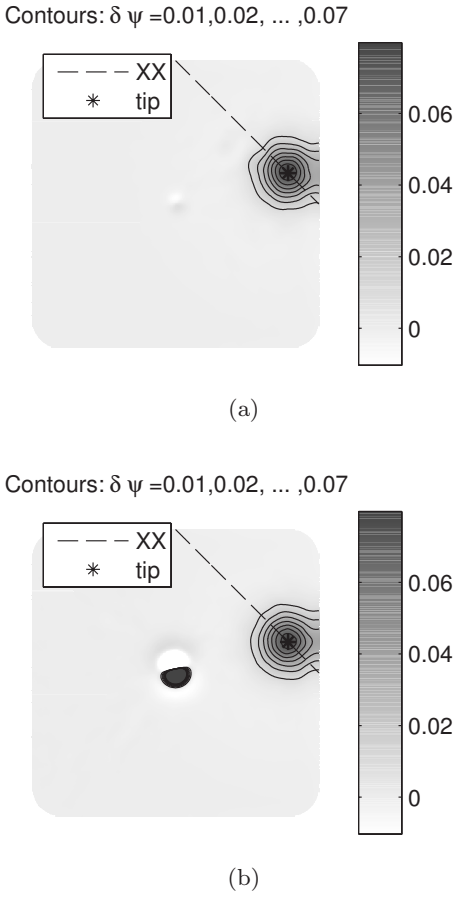

FIG. 4. Comparison of the calculated out of plane rotation, $\delta\psi$, due to the tip field as obtained from the linearized model and the full micromagnetic model. The tip position is marked with a black ⋆ (x_{tip}/a=0.39, y_{tip}/a=0.11, z_{lift}=40 nm). (a) Linearized model. (b) Full model.

λ appears in the linear equations (see Appendix A). It is plotted for the ground state in Fig. 6(c). The predicted MFM scan is shown in Fig. 6(e). Figure 6(f) shows the MFM scan

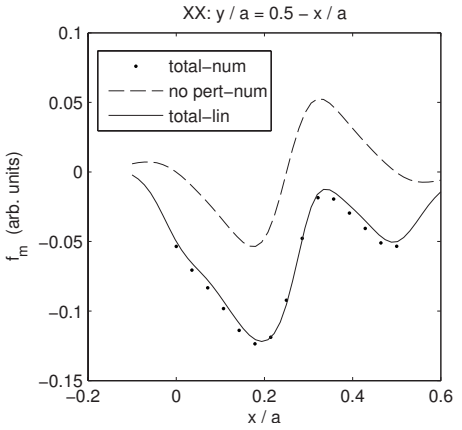

FIG. 5. Comparison between tip force for z_{lift}=40 nm calculated using the full numerical model (num) and linearized approximation (lin) along the cross section (XX) shown as a black dashed line in Fig. 4. Both the total tip force and the perturbation free components are plotted.

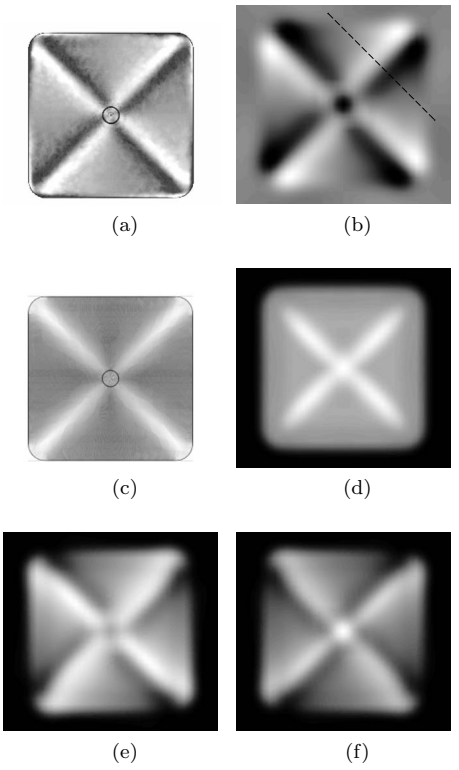

FIG. 6. MFM simulation for the 500 nm square permalloy magnet (z_{lift}=40 nm) and related scalar fields. (a) ρ_m for $\mathbf{M}_0$. (b) f'_m no perturbation. (c) λ for $\mathbf{M}_0$. (d) f'_m induced. (e) Total f'_m. (f) Total f'_m-reversed chirality and polarity.

for a vortex state with reversed chirality and core polarity such that magnetization circulates in a clockwise direction outside the core and upwards within the core. An experimental MFM image for this geometry is shown in Fig. 9(a).

The relationship between Figs. 6(a) and 6(b) is consistent with the interpretation of MFM as a charge mapping technique. The induced signal in Fig. 6(d) shows regions where the tip is above the sample as these appear gray. In this way the induced signal describes the geometry of the sample. The brightest regions of the induced signal coincide with the Neel walls in the unperturbed state which extend along the sample diagonals. The relationship between Figs. 6(c) and 6(d) is discussed in Sec. VI B.

The tendency of MFM measurements to observe an apparent curvature of domain walls, which is independent of scan direction, is present in Fig. 6(e). The independence of scan direction is guaranteed since Fig. 6(e) was predicted by a linear and hence reversible model. The artifact was compared to that of a four bladed propeller in Ref. 11. The white contrast corresponds to the blades of this "propeller" the ends of which curve round in an anticlockwise direction. This is the same direction as the circulation of the magnetization around the vortex core. Comparison of Figs. 6(e) and 6(f) confirms that the sense of the curvature is related to what is conventionally termed the chirality of the ground-state magnetization.

B. Vortex state on an indented rectangle

Figure 7 shows the unperturbed vortex state on an indented rectangle. The structure has a width of 500 nm, a

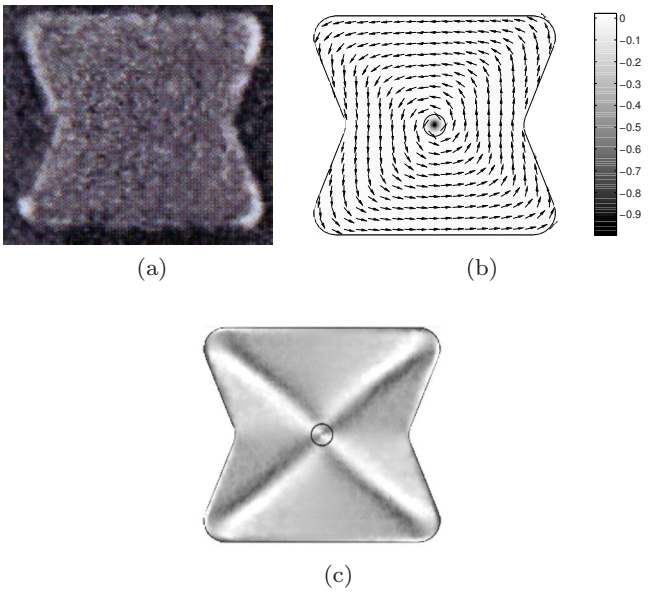

FIG. 7. (Color online) Geometry and ground state of the indented rectangle (width=500 nm, thickness=20 nm, indentation=100 nm). (a) SEM image of geometry. (b) Equilibrium magnetization for $\mathbf{B}^{(app)}=0$ (color map: M_z/M_s, arrows: $\mathbf{M}_0$). (c) ρ_m for $\mathbf{M}_0$.

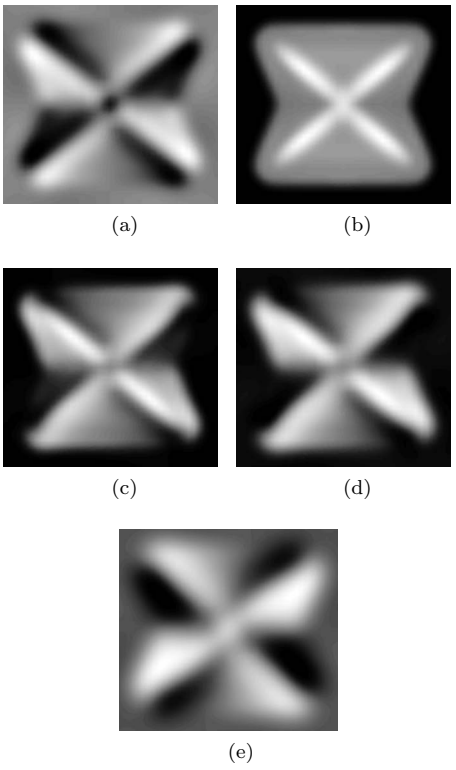

FIG. 8. Simulated MFM images for the indented rectangle (width=500 nm, thickness=20 nm, indentation=100 nm) at various lift heights. (a) f'_m no perturbation, $z_{lift}=40$ nm. (b) f'_m induced, $z_{lift}=40$ nm. (c) f'_m total, $z_{lift}=40$ nm. (d) f'_m total, $z_{lift}=50$ nm. (e) f'_m total, $z_{lift}=80$ nm. Vortex chirality and polarity reversed compared to Fig. 7(b).

thickness of 20 nm and an indent as defined in Fig. 2 of 100 nm. The chamfer due to the lithography process visible in Fig. 7(a) was reproduced in the geometry used in the numerical model [Fig. 7(b)]. The density of magnetic charges corresponding to the magnetization shown in Fig. 7(b) is reproduced for reference in Fig. 7(c).

Figure 8 contains simulated MFM scan results for an indent of 100 nm. Figures 8(a) and 8(b) show the two components of the MFM scan for a lift height of 40 nm. Figures 8(c)–8(e) show simulations of the MFM scan at lift heights of 40, 50, and 80 nm. The results in Fig. 8(e) are for an unperturbed magnetization whose sense is reversed ($\mathbf{M}=-\mathbf{M}_0$) relative to that shown in Fig. 7(b). Experimental MFM images for indents ranging from 0 to 150 nm are shown in Fig. 9.

Through comparison of the experimental images with the simulation results it can be concluded that the indented rectangles are all in the vortex state. The numerical simulations correctly predict the strengthened (brighter) contrast on one out of the two diagonals of the indented prisms in Fig. 9. This arises because the surface charges of the unperturbed state, which are deposited on the indented edge, re-enforce the induced component of the contrast of Fig. 8(b). The vortex chirality determines which of the two diagonals has this re-enforced contrast. The difference in the scan on the pair of nanomagnets shown in Fig. 9(d) can be attributed to their opposite chirality. By comparing Fig. 9(c) with the simulation result of Fig. 8(e) it can be determined that the magnetization imaged in Fig. 9(c) circulates the core in a clockwise direction. It can be seen that the experimental results agree best with the simulations at lift heights of 40–50 nm. The effect of varying the lift height is treated more systematically in Sec. V C.

C. Dependence on z_{lift}

Figures 10(a) and 10(b) show the simulated variation in f'_m along the cross section ($x+y=0.5a$) marked in Fig. 6(b) for the 500 nm square magnet. This cross section intersects a Neel wall in the unperturbed magnetization state at 90°. The curves have been normalized such that the peak value of the curve is unity in each case. Results for lift heights of 40 and 80 nm are shown. The simulated MFM scan at a lift height of 80 nm is shown in Fig. 11.

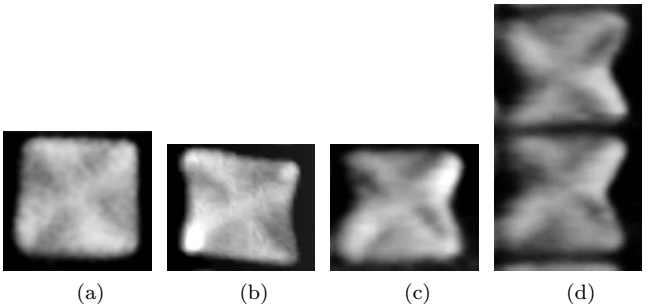

FIG. 9. Experimental MFM images of indented prisms (width =500 nm, thickness=20 nm). The scan direction is horizontal with the exception of Fig. 9(b) where it is vertical. (a) indent =0 nm. (b) indent=50 nm. (c) indent=100 nm. (d) indent =150 nm.

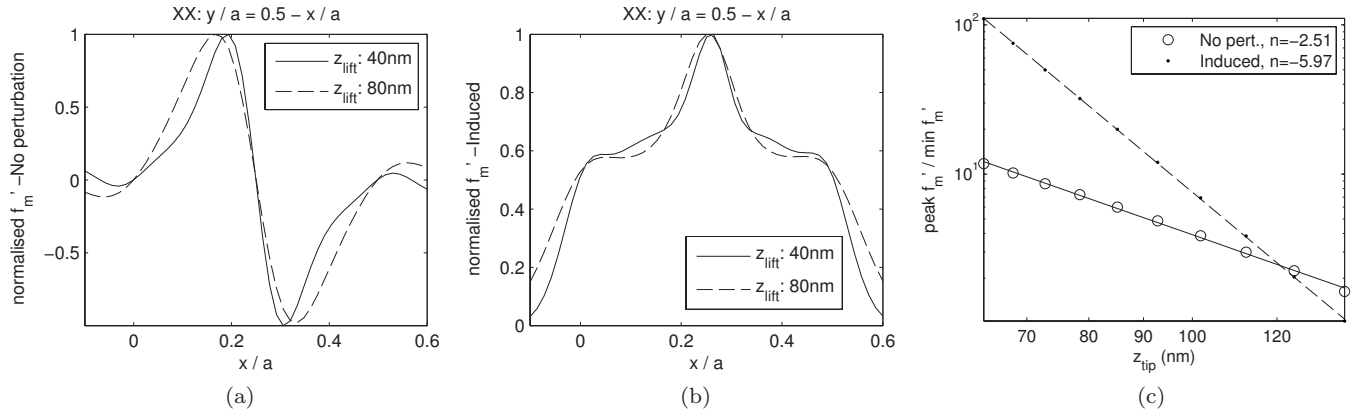

FIG. 10. Simulated value of induced and perturbation free force gradient along the cross section $y+x=0.5a$ [see dashed line of Fig. 6(b)] for the 500 nm square magnet. (a) No perturbation. (b) Induced signal. (c) log-log plot of peak value of f'_m on cross section vs z_{lift}, minimum detectable force gradient (min f'_m) calculated for $Q=300$, $\Theta=300$ K, $k_{can}=1.5$ Nm^{-1}, and $\sqrt{\langle y_D^2 \rangle}=5$ nm.

The dependence of the peak value of f'_m on lift height is shown in Fig. 10(c). The lift height has been quantified in terms of z_{tip} whose relationship with z_{lift} is shown in Fig. 1. The value of f'_m has been scaled by the minimum detectable f'_m calculated from Eq. (11). A fit of the form $f'_m=Az_{tip}^n$ has been plotted alongside the simulation data.

The induced signal drops much more rapidly with lift height than the perturbation free signal. The faster drop of the induced signal with increasing lift height arises because not only does the strength of the field at the tip height fall but also the strength of the perturbation. For tip heights of 120 nm ($z_{lift} \simeq 80$ nm) and above both signals disappear into the thermal noise. The simulated data is fitted reasonably well by the power law.

VI. DISCUSSION

A. Vortices in indented rectangles

The previous section presented measurements on 500-nm-wide, 20-nm-thick structures with indents from 0 nm up to 150 nm. All of these where found to be in the vortex state. It is interesting to compare this finding with the results reported in Ref. 12. Increasing sample thickness will favor vortex states over uniform states. Thus it can be inferred from the phase diagram for 10-nm-thick indented rectangles of Ref. 12 that the lowest energy or ground state for our 20-nm-thick structures will be a vortex. Thus our finding is not remarkable except that all of the thinner structures investigated in Ref. 12 exhibited a remnance under zero applied field of at least 60% of saturation. This is despite the fact that for most of these thinner structures the lowest energy state was a vortex. Thus increasing the thickness to 20 nm was sufficient to cause the nucleation of a vortex in the absence of an applied field. The longer time scale for our measurement may also have been a contributing factor in the nucleation of the vortex state. Additionally the MFM approach was capable of determining the chirality of the vortex ground state, something which could not have been inferred from a magnetometry measurement of zero remnance.

B. Induced contrast

There is a correlation between the induced contrast seen in Fig. 6(d) and the distribution of $\lambda=-M_{x0}H_{x0}^{(m)}-M_{y0}H_{y0}^{(m)}$ in the ground state shown in Fig. 6(c). Figure 12 provides an additional example of such correlation for the flower state on a 300 nm indented rectangle [see Fig. 12(a)]. The distribution of λ and the induced component of the MFM scan are shown in Figs. 12(b) and 12(c), respectively.

The relationship can be understood qualitatively in the following way. The induced signal is larger when the magnetization beneath the tip is more easily perturbed by the applied tip field. The magnetostatic interaction seeks to align magnetic dipoles with the local **H** field. In regions where the magnetization is aligned antiparallel to a strong **H** this magnetostatic interaction "softens" the magnetization distribution and increases the degree of perturbation. This effect is second order in energy and hence first order in the first variation. As such it appears in the coefficient of the $\delta\theta$ and $\delta\psi$ terms in Eqs. (A1) and (A2), respectively. The induced contrast will decrease moving into the corners of the sample since changes to the magnetization here deposit surface charges which discourage further induced rotation. This effect is visible in Figs. 6(d) and 12(c).

It can be noted that the large value of λ coincided with regions of high ρ_m in the vortex state. This is because the stray field will be large near such magnetic charges and $|\mathbf{M}|$

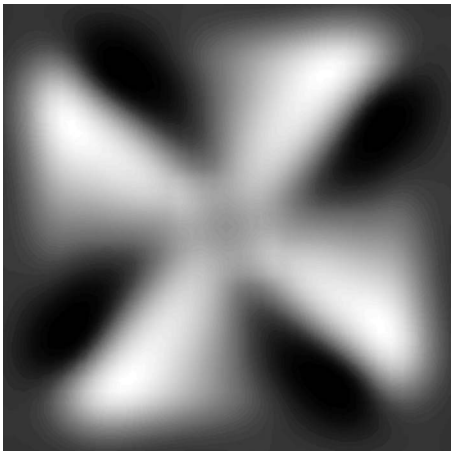

FIG. 11. Simulated MFM image for the 500 nm square at a lift height of 80 nm.

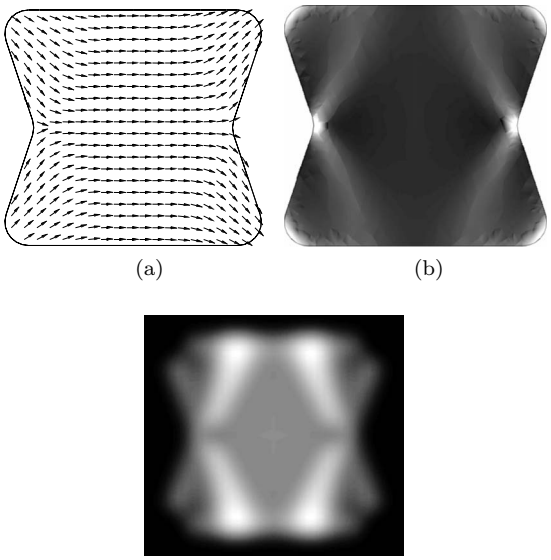

(a) (b) (c)

FIG. 12. Induced contrast in the flower state on an indented rectangle (width=300 nm, indent=50 nm, thickness=20 nm) for z_{lift}=40 nm. (a) Equilibrium state $\mathbf{M}_0$. (b) λ for $\mathbf{M}_0$. (c) Induced f'_m.

is constrained to be constant. Consequently strong induced MFM contrast can be expected in regions that have strong magnetic charge contrast. The induced contrast will act to re-enforce the contrast from positive magnetic charges. This effect is visible in Fig. 6(e) and is consistent with the general finding that one sign of contrast is favored in MFM images.

The decomposition of the total MFM signal [Fig. 6(e)] into perturbation free and induced components helps to explain the observed curvature of the wall. Both components exhibit a symmetry however, as can be seen in Figs. 10(a) and 10(b), one is asymmetric while the other is symmetric about the center of the Neel wall. Where the induced component of the signal is strong it acts to shift the peak toward the center of the Neel wall. However, moving outwards from the vortex core the strength of the induced contrast falls. As a result the peak in signal strength on a given line scan moves away from the center of the wall and toward the peak on the perturbation free scan. Figure 13 shows the tip induced change to the in-plane component of magnetization $\delta\theta$, as calculated by the linear model, for a tip at the position marked by an asterisk. The position of the Neel wall with and without the tip, as quantified by the contour $\theta=\frac{3\pi}{4}$, is also shown. From this figure it can be confirmed that the observed wall curvature from the MFM scan in no way corresponds to the curvature adopted as a result of perturbation by the tip.

Figures 8(e) and 11 show simulations, which due to the high lift height, have a much weaker induced contribution to the contrast. The propeller curvature of the white contrast is still visible. Importantly, however, the relationship with the underlying vortex chirality is reversed. The ground state magnetization for Fig. 8(e) circulates the core in a clockwise direction. However, the ends of the propeller curve round in an anticlockwise direction. It is this form of curvature which is visible in the experimental MFM images of Figs.

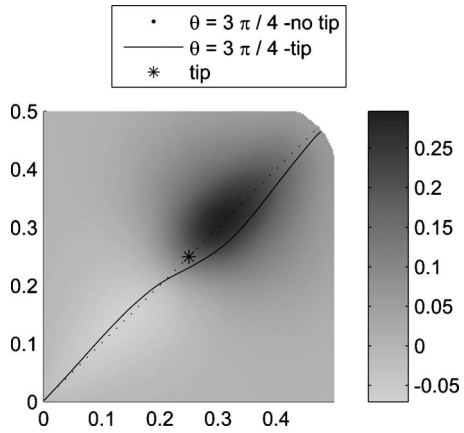

FIG. 13. Simulated movement of Neel wall ($\theta=\frac{3\pi}{4}$) in upper right quadrant of 500 nm square structure due to tip ($x_t/a=y_t/a=0.25$, z_{lift}=40 nm). The color map shows the change to the in-plane magnetization direction ($\delta\theta$).

9(b)–9(e). Attempting to apply the relationship between tip curvature and vortex chirality obtained from Fig. 6 to these images would result in an incorrect determination of the chirality. Correct chirality identification is important given the potential for information storage in vortex states.

C. Optimal operation

Both the induced and zero-order components of the MFM signal are related to the ground state magnetization. We argued in the previous section that it is possible to predict qualitatively the relationship between the ground state magnetization and induced contrast. However, the induced contrast, unlike the perturbation free signal, does not discriminate between the case where $\mathbf{M}=\mathbf{M}_0$ and $\mathbf{M}=-\mathbf{M}_0$ (at least to linear order where no external fields are applied to the sample). As such it is desirable to maximize

$$R=\frac{f'_{m0}}{f'_{mi}}, \tag{16}$$

where f'_{m0} is the perturbation free signal and f'_{mi} is the induced scan signal.

From Figure 10(c) it can be seen that R increases with increasing lift height. Using a larger lift height will reduce the image resolution. However, as can be seen from Figs. 10(a) and 10(b) the peak width increases by less than 50% for a doubling of the lift height. A more critical limitation on lift height is the thermal noise, which acts to limit the maximum possible z_{lift}. The level of thermal noise could be reduced by operation in a moderate vacuum although this would impact the bandwidth and hence acceptable scan rate. Vacuum operation would also limit sample access.

An alternative to vacuum operation is to change the tip moment. Assuming the linearization of the perturbation problem remains accurate the induced scan signal $f'_{mi}\propto m_0^2$ while the charge contrast or perturbation free signal has the dependence $f'_{m0}\propto m_0$. Adopting the power law fit to peak signal strength of Sec. V C

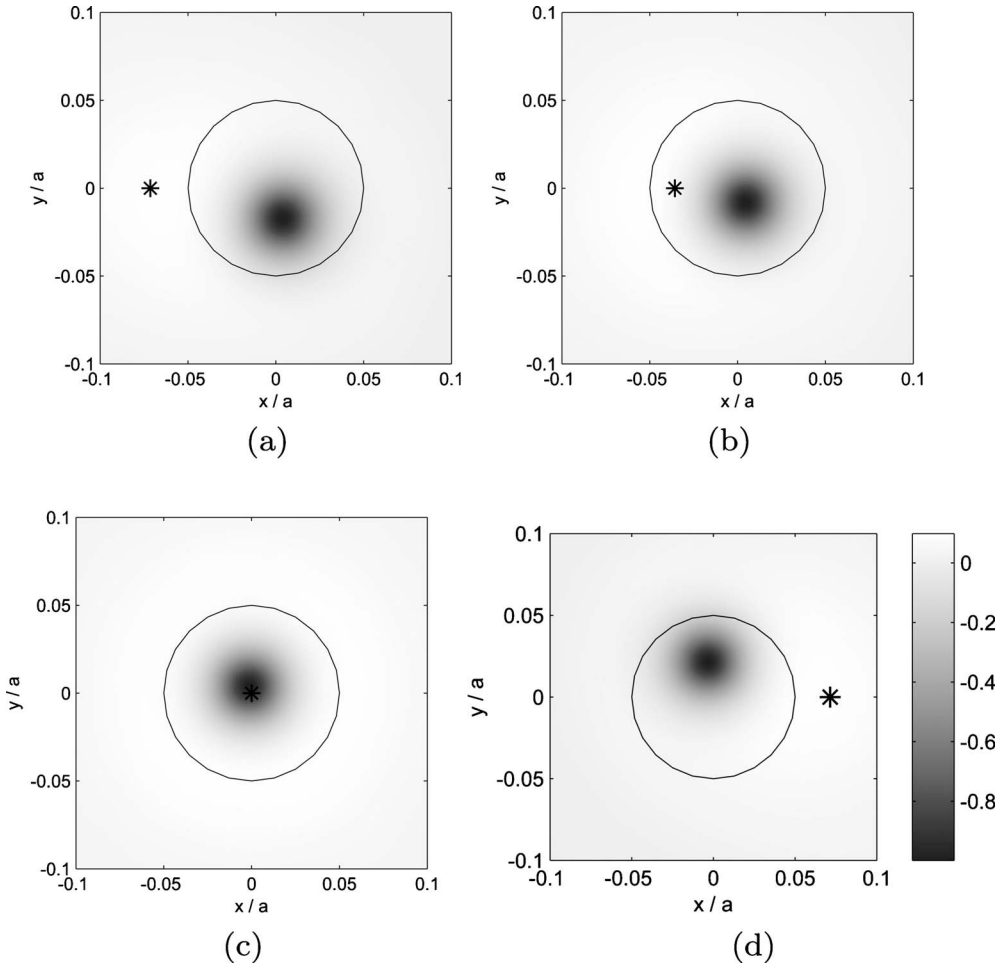

FIG. 14. Color map of M_z/M_s for various stages in a scan of the tip along the line $y=0$. Results calculated using the full numerical model for the 500 nm square magnet. Tip parameters: $z_{lift}=40$ nm and $V_{eff}=10^5$ nm^3. The tip location, $\mathbf{x}_t$, is marked with a black asterisk. (a) $x_t/a=-0.07$. (b) $x_t/a=-0.04$. (c) $x_t/a=0.00$. (d) $x_t/a=0.07$.

$$\frac{f'_{m0}}{f'_{m\ \text{noise}}} = \beta_0 m_0 z_{tip}^{-n_0}, \tag{17}$$

$$\frac{f'_{mi}}{f'_{m\ \text{noise}}} = \beta_i m_0^2 z_{tip}^{-n_i}. \tag{18}$$

The constraint on lift height can be stated as $f'_{m0} \geq r f'_{m\ \text{noise}}$, where r is some positive constant describing the detection threshold. This leads to the constraint

$$z_{tip} \leq \left(\frac{\beta_0 m_0}{r}\right)^{1/n_0}. \tag{19}$$

Thus the maximum value of $R=\hat{R}$ is

$$\hat{R} = \frac{\beta_0^{(n_i/n_0)}}{\beta_i r^{(n_i/n_0)-1}} m_0^{(n_i/n_0)-2}. \tag{20}$$

When $n_i=2n_0$, $\hat{R}$ will have no dependence on tip moment. For the values obtained for a scan on the Neel wall $\hat{R} \propto m_0^{0.4}$. Thus using large tip moments should be conducive to good observation of magnetic charge contrast for vortex states. For the two pass technique, however, using a high moment tip during the topographic scan could switch the sample magnetization invalidating the measurement.[32]

The tip's effective volume corresponded to a sphere 30 nm in radius. The spatial variation of $\frac{\partial^2 H_z}{\partial z^2}$ was limited by the lift height needed to prevent induced contrast dominating the scan signal and the strength of exchange interaction in Permalloy. Hartmann[21] showed that provided the diameter of the magnetic volume did not exceed the peak width of the signal the point dipole approximation did not introduce noticeable error. This was the case for the signals presented here, a fact that was verified numerically during our simulations. On the basis of this it can be concluded that use of a physically "sharp" tip will not improve resolution.

D. Limitations of the linear model

An important limitation of the linear model is its inability to predict the displacement of a vortex core as a result of the tip field. Figure 14 shows several stages from a full micromagnetic simulation in which the tip was scanned along the line $y=0$. The displacement of the core can be attributed to the in-plane component of the tip field. Figure 15 compares the induced component of the force on the tip as calculated

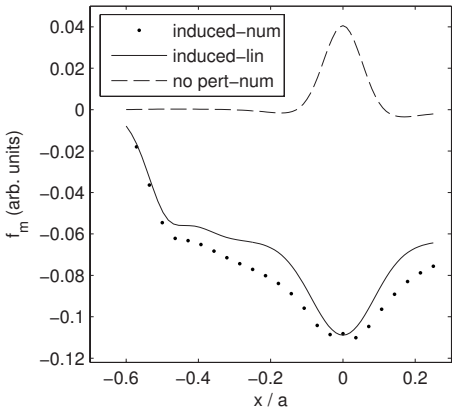

FIG. 15. Comparison of induced tip force as calculated by the full num and lin models on the cross section $y_{tip}=0$, $z_{lift}=40$ nm. The tip force in the absence of perturbation is also plotted.

by the full micromagnetic model and the linear model as the tip scans this line. We attribute the error from the linear model visible in this figure to the core displacement. When $x_{tip}=0$ or is large the core is centered and the linear prediction is in good agreement with the full micromagnetic model. This was the case for the results presented in Fig. 5. Even when the core displacement is moderate the calculated value of the tip force is still predicted to a useful accuracy. This is particularly true given that the simulation results are an aid to interpretation of experimental data. As such a fingerprint showing the general features of the magnetization state is sufficient.

It should also be noted that the linear approximation was found to be inaccurate for certain elongated rectangle geometries. Our numerical simulations predicted that these geometries adopted uniform states that were significantly perturbed by small applied fields. The corresponding experimental MFM measurements yielded images with bright streaks that were difficult to interpret. An analysis of such geometries appears to be beyond our current experimental and numerical setup and as such no results for these geometries have been presented in this paper.

VII. CONCLUSION

A linear approximation to the equations of micromagnetics can efficiently predict the contribution of tip-sample perturbation to MFM measurements. This numerical technique was successfully combined with experiment in the study of 20-nm-thick indented prisms. It was found that even for indents of 150 nm a vortex state nucleated from the saturated state in the absence of an applied field. This is in contrast to the behavior of the 10-nm-thick structures studied previously. The combined MFM technique was further able to identify the chirality of the vortex state.

In the thin prismatic structures studied the induced contrast can be explained by the destabilizing influence of the local stray field on the magnetization distribution. Thus it is possible to qualitatively predict the induced contrast from the unperturbed magnetization distribution. The apparent curvature or "propellering" of the Neel walls observed during MFM measurements on vortex states arises from the superposition of the individually straight zero-order and induced wall signatures. The relationship between the apparent wall curvature and vortex chirality depends on the relative strength of the induced contrast. Consequently this wall curvature cannot be used to infer the chirality of vortex states. Optimal observation of Neel walls is achieved at high lift heights where the limitation on achievable lift height comes from the thermal noise and not loss of resolution. The effect of thermal noise can be mitigated, albeit weakly, by using large tip moments.

APPENDIX A: FIRST-ORDER EQUATIONS ON $\delta\theta$ and $\delta\psi$

It is convenient to work in terms of the nondimensional variables, which are used throughout this section. The overbars have been omitted. The equations governing $\delta\theta$ and $\delta\psi$ are

$$\delta\theta{:}\nabla\cdot(-\cos^2\psi_0\nabla\delta\theta+\delta\psi\sin 2\psi_0\nabla\theta_0)-\frac{1}{2A}(\mathbf{H}_0+\delta\mathbf{H}^{(app)})\cdot\mathbf{M}_\theta^{\theta'}\delta\theta=\frac{1}{2A}(\delta\mathbf{H}^{(app)}+\delta\mathbf{H}^{(m)})\cdot\mathbf{M}_0^{\theta'}+\frac{1}{2A}(\mathbf{H}_0+\delta\mathbf{H}^{(app)})\cdot\mathbf{M}_\psi^{\theta'}\delta\psi, \tag{A1}$$

$$\delta\psi{:}\nabla\cdot(-\nabla\delta\psi)-\left[\cos 2\psi_0|\nabla\theta_0|^2+\frac{1}{2A}(\mathbf{H}_0+\delta\mathbf{H}^{(app)})\cdot\mathbf{M}_\psi^{\psi'}\right]\delta\psi=\frac{1}{2A}(\delta\mathbf{H}^{(app)}+\delta\mathbf{H}^{(m)})\cdot\mathbf{M}_0^{\psi'}+\frac{1}{2A}(\mathbf{H}_0+\delta\mathbf{H}^{(app)})\cdot\mathbf{M}_\theta^{\psi'}\delta\theta, \tag{A2}$$

where

$$\mathbf{M}_0^{\theta'}=(-\sin\theta_0\cos\psi_0,\cos\theta_0\cos\psi_0,0),$$

$$\mathbf{M}_\theta^{\theta'}=(-\cos\theta_0\cos\psi_0,-\sin\theta_0\cos\psi_0,0),$$

$$\mathbf{M}_\psi^{\theta'}=(\sin\theta_0\sin\psi_0,-\cos\theta_0\sin\psi_0,0),$$

$$\mathbf{M}_0^{\psi'}=(-\cos\theta_0\sin\psi_0,-\sin\theta_0\sin\psi_0,\cos\psi_0),$$

$$\mathbf{M}_\theta^{\psi'}=(\sin\theta_0\sin\psi_0,-\cos\theta_0\sin\psi_0,0),$$

$$\mathbf{M}_\psi^{\psi'}=(-\cos\theta_0\cos\psi_0,-\sin\theta_0\cos\psi_0,-\sin\psi_0)$$

$\delta\theta$ is subject to the boundary condition

$$\cos^2\psi_0\nabla\delta\theta\cdot\mathbf{n}=0, \tag{A3}$$

where $\mathbf{n}$ is a unit vector normal to the surface $\partial\Omega_m$. Likewise $\delta\psi$ is subject to the boundary condition

$$\nabla\delta\psi\cdot\mathbf{n}=0. \tag{A4}$$

APPENDIX B: NOISE LIMIT FOR MEASUREMENT OF PHASE SHIFT

The gradient of the magnetic force along the axis of tip oscillation, f'_m alters the effective stiffness of the beam, k_{can}. For a constant drive frequency this results in a phase shift of $\varphi = Qf'_m/k_{can}$, where Q is the Q factor of the cantilever. The phase signal is obtained from the tip displacement using a mixer and subsequent low pass filter to remove harmonics on the order of the drive frequency and above. The output signal is given by

$$V_\varphi = \alpha \frac{y_D}{2} \frac{Q}{k_{can}} f'_m, \tag{B1}$$

where y_D is the tip oscillation amplitude and α is the detector sensitivity.

Where the MFM equipment is operated at atmospheric pressure the Q factor is on the order of 300 and the dominant noise source is due to the fluctuations in this dissipation mechanism.[16] The transfer function, $A(\omega)$ relating the noise force to the output of the demodulation circuit V_p is

$$A(\omega) = \alpha F(\omega)[G(\omega - \omega_d) - G(\omega + \omega_d)], \tag{B2}$$

where ω_d is the drive frequency, $F(\omega)$ is the transfer function of the low pass filter and $G(\omega)$ is the response function for the cantilever. The expectation of the mean squared signal over a duration T_0 is in the limit[33]

$$\lim_{T_0 \to 0} \langle \overline{V_p^2(t)} \rangle = \int_{-\infty}^{\infty} |A(\omega)|^2 d\omega \psi \tag{B3}$$

$\langle\ \rangle$ denotes an ensemble average while the overbar denotes a time average. The spectral density function of the noise force is: $\psi = 2\lambda k_B \Theta$, where λ is the damping coefficient, k_B is Boltzmann's constant and Θ the temperature.

The cantilever responds to changes in the drive frequency with respect to its resonant frequency on a time scale, $\tau_{can} = \frac{2Q}{\omega_n}$. Assuming the cantilever drive frequency equals the cantilever resonant frequency and modeling the filter as a critically damped second order system with cutoff frequency $\frac{1}{\tau_{can}}$

$$|A(\omega)|^2 \simeq \frac{1}{k_{can}^2} \frac{(2Q)^2}{[1 + (2Q\omega/\omega_0)^2]^3}. \tag{B4}$$

The rms value of the noise voltage in the phase signal is therefore

$$V_p^{(\text{rms noise})} = \frac{\alpha}{2} \sqrt{\frac{3\pi}{2k_{can}} k_B \Theta}. \tag{B5}$$

Taking the detection limit as the case where $V_p^{(\text{rms noise})} = V_\varphi$ then the minimum detectable force gradient is

$$f'_{\min} = \frac{1}{y_D Q} \sqrt{\frac{3\pi}{2} k_{can} k_B \Theta}. \tag{B6}$$

For the phase detection technique, the cantilever is driven on resonance thus to first order the oscillation amplitude is unaffected by changes in the natural frequency.

*Corresponding author; cd229@cam.ac.uk

[1] S. Tehrani, J. Slaughter, M. Deherrera, B. Engel, N. Rizzo, J. Salter, M. Durlam, R. Dave, J. Janesky, B. Butcher, K. Smith, and G. Grynkewich, Proc. IEEE **91**, 703 (2003).

[2] R. P. Cowburn and M. E. Welland, Science **287**, 1466 (2000).

[3] B. Van Waeyenberge, A. Puzic, H. Stoll, K. W. Chou, T. Tyliszczak, R. Hertel, M. Fähnle, H. Brückl, K. Rott, G. Reiss, I. Neudecker, D. Weiss, C. H. Back, and G. Schütz, Nature (London) **444**, 461 (2006).

[4] J. I. Martín, J. Nogués, K. Liu, J. L. Vicent, and I. K. Schuller, J. Magn. Magn. Mater. **256**, 449 (2003).

[5] R. Wiesendanger, *Scanning Probe Microscopy and Spectroscopy: Methods and Applications* (Cambridge University Press, Cambridge, 1994).

[6] O. Klein, G. de Loubens, V. V. Naletov, F. Boust, T. Guillet, H. Hurdequint, A. Leksikov, A. N. Slavin, V. S. Tiberkevich, and N. Vukadinovic, Phys. Rev. B **78**, 144410 (2008).

[7] J. N. Chapman and M. R. Scheinfein, J. Magn. Magn. Mater. **200**, 729 (1999).

[8] M. R. Scheinfein, J. Unguris, D. T. Pierce, and R. J. Celotta, J. Appl. Phys. **67**, 5932 (1990).

[9] A. Hubert, W. Rave, and S. L. Tomlinson, Phys. Status Solidi B **204**, 817 (1997).

[10] S. L. Tomlinson and E. W. Hill, J. Magn. Magn. Mater. **161**, 385 (1996).

[11] J. M. García, A. Thiaville, J. Miltat, K. J. Kirk, J. N. Chapman, and F. Alouges, Appl. Phys. Lett. **79**, 656 (2001).

[12] D. K. Koltsov and M. E. Welland, J. Appl. Phys. **94**, 3457 (2003).

[13] J. D. Jackson, *Classical Electrodynamics*, 3rd ed. (Wiley, New York, 1999).

[14] A. Aharoni, *Introduction to the Theory of Ferromagnetism* (Oxford Science Publications, Oxford, 1996).

[15] D. Rugar, H. J. Mamin, P. Guethner, S. E. Lambert, J. E. Stern, I. McFadyen, and T. Yogi, J. Appl. Phys. **68**, 1169 (1990).

[16] T. R. Albrecht, P. Grutter, D. Horne, and D. Rugar, J. Appl. Phys. **69**, 668 (1991).

[17] V. Mironov, D. Nikitushkin, C. Binns, A. Shubin, and P. Zhdan, IEEE Trans. Magn. **43**, 3961 (2007).

[18] M. R. Koblischka, U. Hartmann, and T. Sulzbach, Proceedings of Symposium J on Growth and Evolution of Ultrathin Films: Surface and Interface Geometric and Electronic Structure, of the E-MRS Spring Conference, Thin Solid Films **428**, 93 (2003).

[19] We certainly do not wish to imply there is anything wrong with methods based on the value of the functional provided the considerations outlined in Ref. 11 are taken into account. We just preferred a different approach.

[20] The suffix notation is preferred to the use of the ∇ operator employed in Ref. 13 since in the continuum limit $\mathbf{m} \to \mathbf{M}dV$ and $\mathbf{M}$ is a function of position.

[21] U. Hartmann, Phys. Lett. A **137**, 475 (1989).
[22] The surface integral is preferable as numerically it scales as $\mathcal{O}(N^{2/3})$.
[23] C. J. García-Cervera, Z. Gimbutas, and Weinan E, J. Comput. Phys. **184**, 37 (2003).
[24] H. C. Martin and G. F. Carey, *Introduction to Finite Element Analysis*, 1st ed. (McGraw-Hill, New York, 1973).
[25] T. R. Koehler, Physica B **233**, 302 (1997).
[26] J. K. Ha, R. Hertel, and J. Kirschner, Phys. Rev. B **67**, 224432 (2003).
[27] W. Scholz, Ph.D. thesis, Technical University of Vienna, 2003.
[28] P. Asselin and A. A. Thiele, IEEE Trans. Magn. **22**, 1876 (1986).
[29] D. R. Fredkin and T. R. Koehler, J. Appl. Phys. **63**, 3179 (1988).
[30] E. M. Freeman and D. A. Lowther, IEEE Trans. Magn. **25**, 4135 (1989).
[31] W. Scholz, K. Y. Guslienko, V. Novosad, D. Suess, T. Schrefl, R. W. Chantrell, and J. Fidler, Proceedings of the 4th International Conference on Fine Particle Magnetism (ICFPM), J. Magn. Magn. Mater. **266**, 155 (2003).
[32] V. L. Mironov, B. A. Gribkov, A. A. Fraerman, S. A. Gusev, S. N. Vdovichev, I. R. Karetnikova, I. M. Nefedov, and I. A. Shereshevsky, J. Magn. Magn. Mater. **312**, 153 (2007).
[33] C. V. Heer, *Statistical Mechanics, Kinetic Theory and Stochastic Processes* (Academic Press, London, 1972).